

Article

Facile NiO_x Sol-Gel Synthesis Depending on Chain Length of Various Solvents without Catalyst for Efficient Hole Charge Transfer in Perovskite Solar Cells

Byung Gi Kim, Woongsik Jang and Dong Hwan Wang * 

School of Integrative Engineering, Chung-Ang University, 84 Heukseok-Ro, Dongjak-gu, Seoul 06974, Korea; ayct88@hanmail.net (B.G.K.); dndt1r2@cau.ac.kr (W.J.)

* Correspondence: king0401@cau.ac.kr; Tel.: +82-2-820-5074

Received: 30 September 2018; Accepted: 1 November 2018; Published: 6 November 2018



Abstract: Nickel oxide (NiO_x)-based perovskite solar cells (PSCs) have recently gained considerable interest, and exhibit above 20% photovoltaic efficiency. However, the reported syntheses of NiO_x sol-gel used toxic chemicals for the catalysts during synthesis, which resulted in a high-temperature annealing requirement to remove the organic catalysts (ligands). Herein, we report a facile “NiO_x sol-gel depending on the chain length of various solvents” method that eschews toxic catalysts, to confirm the effect of different types of organic solvents on NiO_x synthesis. The optimized conditions of the method resulted in better morphology and an increase in the crystallinity of the perovskite layer. Furthermore, the use of the optimized organic solvent improved the absorbance of the photoactive layer in the PSC device. To compare the electrical properties, a PSC was prepared with a p-i-n structure, and the optimized divalent alcohol-based NiO_x as the hole transport layer. This improved the charge transport compared with that for the typical 1,2-ethanediol (ethylene glycol) used in earlier studies. Finally, the optimized solvent-based NiO_x enhanced device performance by increasing the short-circuit current density (J_{sc}), open-circuit voltage (V_{oc}), and fill factor (FF), compared with those of poly(3,4-ethylenedioxythiophene):poly(styrenesulfonate)-based devices.

Keywords: nickel oxide sol-gel; facile organic solvent synthesis; perovskite solar cells; uniform morphology; electrical property

1. Introduction

Over the past few years, the photovoltaic R&D community has presented a breakthrough in the next generation of energy devices, along with numerous research achievements. This is the perovskite solar cell (PSC), which uses a halogenated perovskite (APbX₃, A = monovalent cation and X = halide) [1]. These solar cells have a power conversion efficiency (PCE (%)) of ~22.7%; among them, the MAPbI₃ (CH₃NH₃PbI₃)-based solar cell has been reported to exhibit an excellent light conversion efficiency [2–7]. PSCs have two types of junctions: p-i-n [8–14] or n-i-p [15], in which the perovskite film is sandwiched between electrons (n) and holes (p). The n-i-p structure-based PSCs using a transparent electron transport layer (ETL) are the most common. Therefore, many studies have reported an n-i-p-type PSC configuration exhibiting the best performance [16,17]. However, studies on the inverted p-i-n junction, with a transparent hole transport layer (HTL), are also important. This is because of the following reasons: (a) high charge transfer between the inorganic HTL/perovskite interface [17–20], (b) suppression of hysteresis in the graph of JV characteristics [21,22] and (c) the cost effectiveness of the device [23–27].

On the other hand, the application of PSCs to determine the role of an inorganic material HTL having inherent photoelectric characteristics and high stability is emerging as an interesting subject [28–32]. Hence, we tried to optimize the synthesis of a spin-coated inorganic metal oxide, nickel oxide (NiO_x), as an HTL applicable to inverted PSCs. It is important to control the stability of the sol, i.e., precipitation, in the synthesis of the sol-gel solution of the nickel precursor.

According to the literature, there are many cases in which bulky alcohols are used to prevent the precipitation of branched nickel precursors [33]. However, in the synthesis of the sol-gel solution, a rapid precipitation of the precursors has been observed in common alcoholic solvents such as ethanol and isopropanol. For example, the use of 2-methoxyethanol (methyl cellosolve) causes precipitation [32,34–36]. It has been observed that the use of the bulky 2-methoxyethanol solvent in the sol does not improve the solution stability at room temperature. Therefore, the precipitates of the nickel precursor could be dissolved only by increasing the temperature [37–41]. In earlier studies, toxic chemicals (monoethanolamine or ethylenediamine, as a typical chelating agent) have also been used to improve the solubility of the sol-gel solution. However, high-temperature annealing was inevitable, to remove the residual organic toxic catalysts in the solution, after synthesis [42–45].

Hence, a divalent alcohol-based solvent (having one more hydroxyl group than a monohydric alcohol-based solvent) was selected to synthesize the NiO_x sol-gel without a toxic catalyst. It was observed that the nickel precursor did not precipitate, and the stability of the solution improved [46–50]. We found that the results of this experiment were based on the evaporation rate effect of the boiling points of the different solvents [51–59]. Finally, we optimized the facile synthesis method of NiO_x sol-gels using dihydric alcohol solvents, such as 1,2-ethanediol (ET-OH), 1,4-butanediol (B-OH) and 1,5-pentanediol (P-OH) (the detailed synthesis procedure is described in the Experimental Section). NiO_x thin films were also prepared using these sol-gels, with three organic solvents having different bond lengths and strengths. Thus, we used the reproducible organic solvent-based synthesis of NiO_x sol-gels, and fabricated PSCs to identify the variation in the photovoltaic parameters. Unlike the previously reported solvents, the new solvent-based NiO_x was applied to an inverted PSC to clearly distinguish the PCE (%) changes. The optimized solvent-based NiO_x improved the device performance by increasing the short-circuit current density (J_{sc}) and open-circuit voltage (V_{oc}), compared with those of poly(3,4-ethylenedioxythiophene):poly(styrenesulfonate)(PEDOT:PSS)-based devices.

2. Materials and Methods

2.1. Material Preparation

The NiO_x solution was synthesized by mixing a certain amount of $\text{Ni}(\text{NO}_3)_2 \cdot 6\text{H}_2\text{O}$ precursor with 1,2-Ethylenediol, 1,4-Butanediol, and 1,5-Pentanediol (All chemicals of NiO_x were purchased from Sigma Aldrich, Saint Louis, MO, USA). For the other hole transport layer (HTL), poly(3,4-ethylenedioxythiophene):polystyrene sulfonate (PEDOT:PSS), AI 4083 was supplied by CLEVIOS™ (Heraeus, Suwon, Korea). For the MAPbI_3 solution, MAI ($\text{CH}_3\text{NH}_3\text{I}$, Dyesol-Timo Co., Ltd., Seongnam, Gyeonggi-do, Korea) and 99.99% lead (II) iodide (TCI Co., Ltd., Taipei, Taiwan) were dissolved and stirred in a mixture of gamma-Butyrolactone (GBL), purchased from Sigma-Aldrich (Saint Louis, MO, USA), and dimethyl sulfoxide (DMSO), purchased from Junsei Co., Ltd. (Tokyo, Japan). All other chemicals were used from Sigma Aldrich.

2.2. NiO_x Sol-Gel Preparation

$\text{Ni}(\text{NO}_3)_2 \cdot 6\text{H}_2\text{O}$ precursor (Sigma-Aldrich, Saint Louis, MO, USA) was used for NiO_x sol-gel synthesis. The nickel precursor (1 M) was mixed with 10 mL of a divalent alcohol solvent of 1,2-ethylenediol (ET-OH), 1,4-butanediol (B-OH), and 1,5-pentanediol. The mixture was stirred at 75 °C for 2 h and then filtered through a 0.25 μm pore filter at room temperature. Three synthesized NiO_x sol-gels were slightly different in color depending on the solvent. The properties of the material

are shown in Table S1, and the NiO_x solution and substrate photographs are shown in Figure S1. Using these materials, the device was fabricated with the composition shown in Figure 1 [60,61].

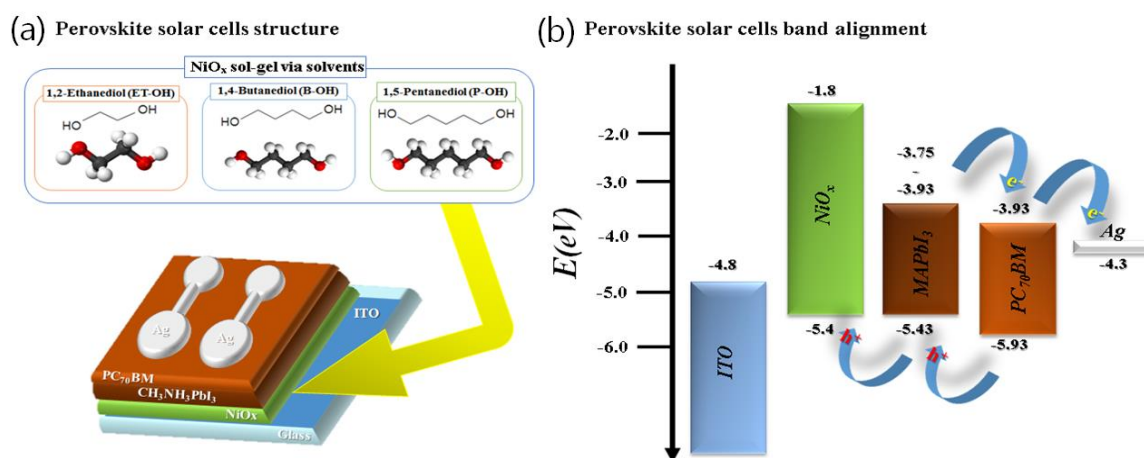


Figure 1. (a) A schematic diagram of an inverted planar perovskite solar cell using a hole transport layer with a NiO_x thin film via solvent. (b) Band energy alignment of the device.

2.3. Thin Films and Device Fabrication

A patterned Indium tin oxide ITO substrate was first washed with solvents, DI water, acetone, and isopropanol and subsequently treated with O_2 -plasma for 15 min. A NiO_x film was spin-coated on the ITO substrate, at 1500 rpm for 60 s, and immediately transferred to a 120 °C hot plate and annealed in air at 300 °C for 1 h. After annealing, a MAPbI_3 layer was deposited under an Ar environment. The MAPbI_3 deposition was optimized by dissolving PbI_2 and MAI solutes at a molar ratio of 1.06:1, a concentration of 1.20 M in Dimethylformamide (DMF):Dimethyl sulfoxide (DMSO), and a volume ratio 7:3.

2.4. Characterization of the Devices

The performances of the PSCs were measured using the PEC-L01 solar simulator (Pecell Technologies, Inc., Kanagawa, Japan), with an air-mass-1.5 global spectrum (AM 1.5 G) at an intensity of 100 mW/cm^2 . This spectrum was calibrated using a silicon reference cell. Furthermore, the current-density/voltage characteristics and impedance of the PSCs were analyzed using the ZIVE SP1 electrical measurement system (WonATech Co., Seoul, Korea). The device area was confirmed to be 0.118 cm^2 , based on the deposited Ag cathode of the mask pattern. The power calibration was measured using an LS150 device (Abet Technologies, Inc., Milford, CT, USA). The incident photon-to-current efficiency (IPCE) was determined using a MonoRa-500i monochromator (DongWoo Optron Co. Ltd., Gwangju, Gyeonggi-do, Korea). The surface morphology of the various thin-film layers were observed using a SIGMA-model scanning electron microscope SEM instrument (Carl Zeiss Inc., San Diego, CA, USA), at 5 kV. The crystallinity of the perovskite layer was analyzed by recording X-ray diffraction (XRD) spectra, using a New D8-Advance (Bruker, Seongnam, Gyeonggi-do, Korea) X-ray diffractometer. Photoluminescence (PL) spectroscopy analysis was performed using a micro-Raman instrument (XperRam 200, Nanobase, Guemcheon-Ku, Korea), with a 550 nm excitation and an incident power of 0.3 mW. Furthermore, the time-resolved photoluminescence (TRPL) was analyzed using a time-correlated single photon counting instrument, with a 454 nm excitation laser and an incident power of 0.3 μW , 25 times the average, 500 ms of exposure time, and 100 ps of resolution. The contact angle of water droplets on “glass/ NiO_x via solvent (ET-OH, B-OH, and P-OH)” were measured with a Phoenix-150 instrument (SEO, Suwon-si, Gyeonggi-do, Korea).

3. Results and Discussion

The two key functions of our device relate to the device fabrication process (Figure 1a,b and Figure S1, and Experimental Section): (i) divalent organic acid-based NiO_x sol-gel synthesis without a catalyst and (ii) thin-film manufacturing process for optimizing the “ NiO_x via solvent/ MAPbI_3 ” interfacial contact.

Figure 2a shows that the NiO_x HTLs (precursor sol, 1 mol/L) prepared with the divalent alcohol-based solvent led to a difference in the JV curve of the PSCs. When the photovoltaic performance analysis (Table 1) was taken into consideration, the V_{oc} of the devices were ~999–1069 mV after 10 min of light-irradiation. The change in the V_{oc} , showing the intrinsic property of the interface quality, was not as high as the ~70 mV for the comparative group. Therefore, the difference in the V_{oc} was not observed to be greatly dependent on the solvent selectivity. On the other hand, a change in the PCE (%) was confirmed by the large differences in the J_{sc} and fill factor (FF). When the PCE (%) was 11.22% and the FF was 62%, the optimized cell corresponded with the NiO_x sol-gel synthesized via B-OH. When NiO_x via ET-OH was used, the J_{sc} was found to be 1.21 mA/cm^2 lower than when the B-OH solvent was used; thus, the J_{sc} was found to depend on the type of sol-gel solvent.

As shown in Figure 2b, the highest IPCE value in the range of 400–650 nm and the integrated J_{sc} (same as $J_{sc,IPCE}$) of 16.79 mA/cm^2 were confirmed for the “ NiO_x via B-OH”-based devices, compared with those of the others. The films of “ NiO_x via solvent” had a similar curvilinear shape for the UV-Vis absorbance spectra (Figure S2a), which signified that the absorbance of the “ NiO_x via B-OH/ MAPbI_3 ” thin film was higher in the range of 400–650 nm than that of the comparative group (Figure S2b).

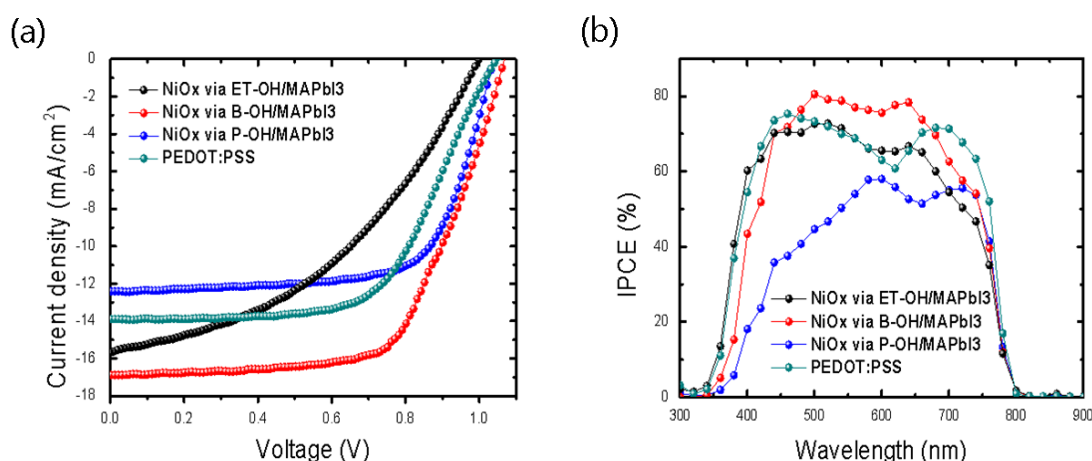


Figure 2. (a) J-V characteristics of inverted PSCs (Perovskite Solar Cells) using sol-gel-based NiO_x transport layers synthesized via three solvents and using PEDOT:PSS (poly (3,4 ethylenedioxythiophene):polystyrene sulfonate); AM 1.5G, 100 mW/cm^2 under solar simulator. (b) IPCE (The incident photon-to-current efficiency) curves of the planar inverted PSC structure.

Table 1. Performance parameters of the planar inverted PSC devices.

HTLs/Parameter	V_{oc}	J_{sc}	$J_{sc,IPCE}$	FF	PCE%
NiO_x via ET-OH	0.999	15.68	15.41	0.42	6.56
NiO_x via B-OH	1.069	16.89	16.79	0.62	11.22
NiO_x via P-OH	1.039	12.42	11.78	0.69	8.91
PEDOT:PSS	0.969	16.18	16.53	0.62	9.74

Field emission scanning electron microscope (FE-SEM) analysis was performed to investigate the difference in morphology among the sol-gel solutions synthesized with divalent alcohol solvents (Figure 3). In the case of “ NiO_x via P-OH” (Figure 3c), the NiO_x sol-gel was formed to a large extent, whereas the rest (Figure 3a,b) had a very flat and uniform substrate [62–64]. It is known that a smooth

and uniform morphology can prevent the aggregation of precursors (accumulation of large amounts of perovskite) [65–68]. In fact, in the case of “NiO_x via B-OH” devices, it was confirmed that the performance of the device was optimal due to the homogeneity of NiO_x. This is because a thin HTL with a uniform coverage of the substrate generally has a low series resistance and an improved shunt resistance [69–71].

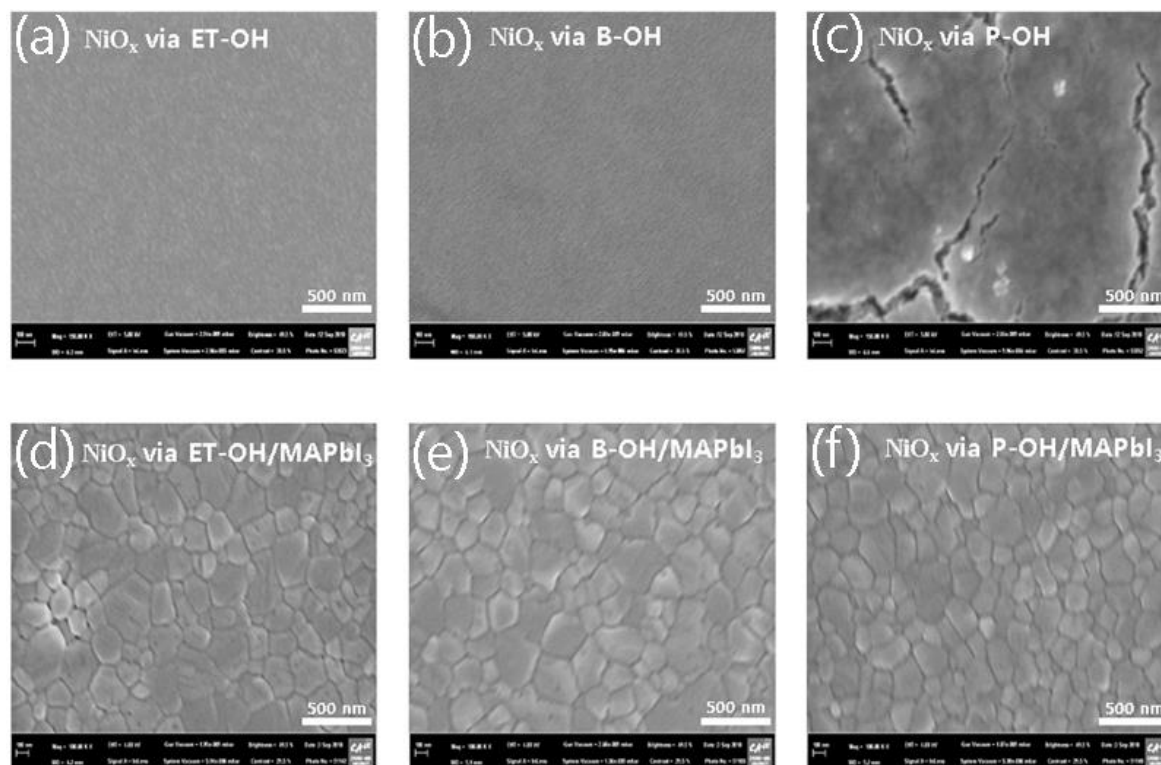


Figure 3. FE-SEM of ITO/NiO_x (sol-gel) via solvent: (a) ET-OH, (b) B-OH, (c) P-OH and MAPbI₃ on ITO/NiO_x (sol-gel) via solvent, (d) ET-OH, (e) B-OH, and (f) P-OH.

As shown in Figure S4, contact angle analysis was performed to compare the NiO_x interfacial state before the deposition of the photoactive layer. The contact angle (Figure S4b) of the “NiO_x via B-OH” thin film (14.42°) was lower than that of the comparative group (Figure S4a,c). This confirmed that the state of this interface was relatively hydrophilic. This result indicates that the “NiO_x via B-OH” substrate is advantageous for interfacial adhesion when a photoactive layer (MAPbI₃) is deposited by spin coating [72,73]. We also confirmed the successful casting of the MAPbI₃ layer on the metal oxide, using the image of the film coverage of NiO_x/MAPbI₃ (Figure 3d–f).

For the quantitative analysis of the previously analyzed nanoporous morphology trends, NiO_x sol-gel substrates were prepared as samples and subjected to XRD analysis (Figure S3). A relatively low full width at half maximum FWHM of 0.248 and nanoporous crystallite size of 373.5 Å were observed for NiO_x via B-OH, compared with those of the comparative group (Table 2). As shown in Figure 4, the XRD spectra of the samples deposited with the photoactive layer showed the sharpest intensity, in the case of the “NiO_x via B-OH” samples. This sample showed the lowest FWHM of 0.103, and the largest crystallite size of 860.6 Å. Therefore, we found that the relatively large grain size of the “NiO_x via B-OH” device was favorable for light absorption, in the comparative group. These results correlate with the higher values of the *J*_{sc}. This is because the perovskite grain acts as a light-absorber, and its absorption depends on the size [74–77].

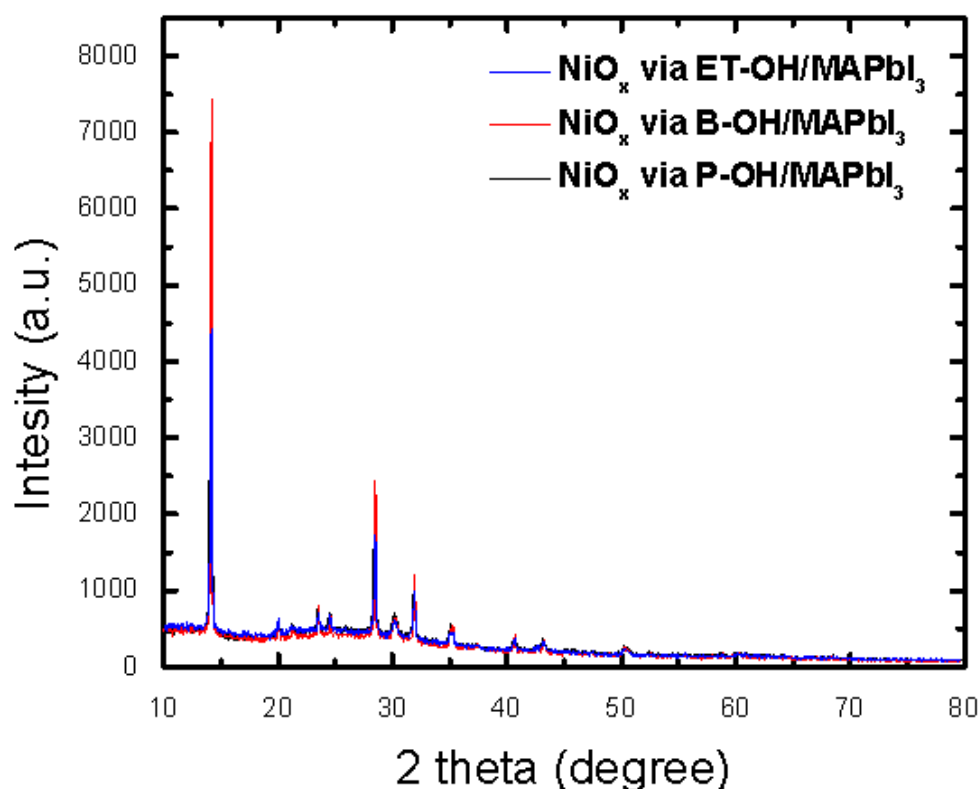


Figure 4. XRD patterns of MAPbI₃ on ITO/NiO_x substrate via solvent (ET-OH, B-OH, and P-OH).

Table 2. Crystallite size with FWHM (Full Width at Half Maximum) on ITO/NiO_x via solvents and ITO/NiO_x via solvents/MAPbI₃ substrate.

Sample Condition	FWHM	C. Size (Å)
ITO/NiO _x via ET-OH	0.285	324.8
ITO/NiO _x via B-OH	0.248	373.5
ITO/NiO _x via P-OH	0.258	358.8
NiO _x via ET-OH/MAPbI ₃	0.252	353.6
NiO _x via B-OH/MAPbI ₃	0.103	860.6
NiO _x via P-OH/MAPbI ₃	0.167	533.6

In addition, electrical property analysis was performed to compare the exciton dissociation (or charge separation) differences. PL analysis was performed with different compositions of the “ITO/NiO_x via solvent (ET-OH, B-OH, and P-OH)/MAPbI₃” samples (Figure 5). We found that the normalized PL intensity was the lowest in the “NiO_x via B-OH” samples. This suggests that the exciton dissociation (or charge separation) tendency of this material is superior [78–81]. It was also found that the PCE (%) values of the devices were consistent with this tendency (Table 1).

Furthermore, in order to compare the electrical properties of the two solvents (ET-OH and B-OH), which resulted in a homogeneous and smooth morphology of the NiO_x thin films, we conducted TRPL analysis of these films, and impedance analysis, through the fabrication of PSCs (Figure 6). The results (Figure 6, Table 3) of the NiO_x via solvent (ET-OH and B-OH) show that the τ_1 , with a charge carrier quenching tendency, was shorter in the B-OH–applied sample, by 1.75 ns. On the other hand, the τ_2 was longer in the ET-OH–applied sample, by 11.5 ns, with a charge-recombination tendency [82–84]. In conclusion, we found a relatively better charge transfer (or charge separation) tendency in the B-OH materials than that of the ET-OH materials, which were commonly used in earlier studies [60,61], because the average τ_{avg} value was shorter in the B-OH samples by 8.83 ns [85–87].

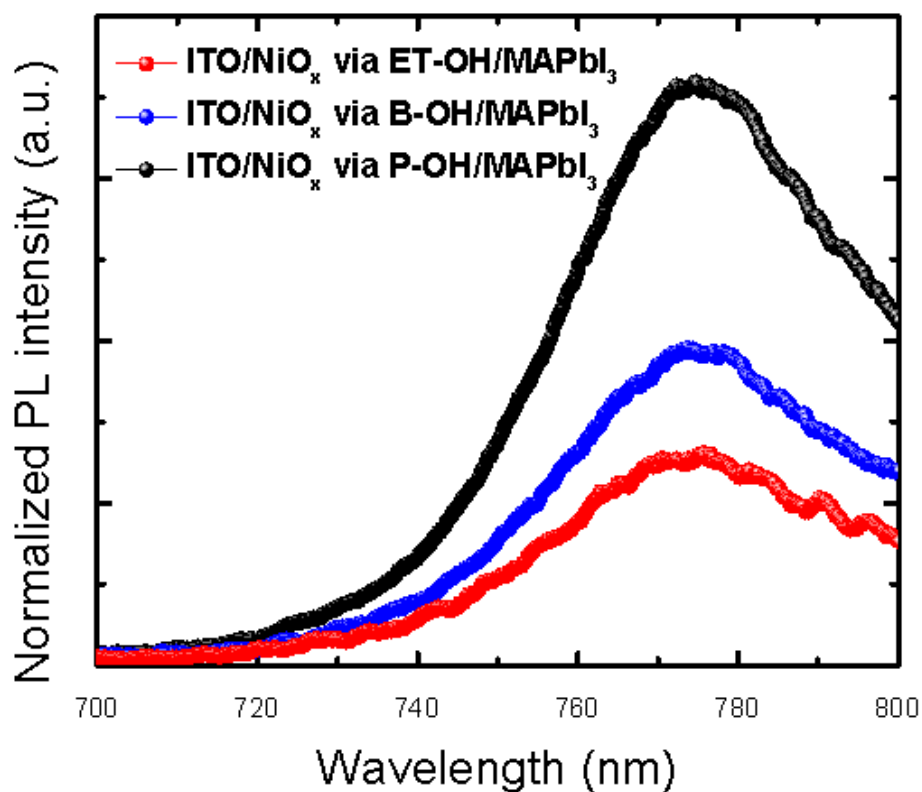


Figure 5. Normalized photoluminescence spectra of the glass/ NiO_x (sol-gel) via solvent (ET-OH, B-OH, and P-OH)/perovskite(MAPbI₃) film under 550 nm light excitation respectively.

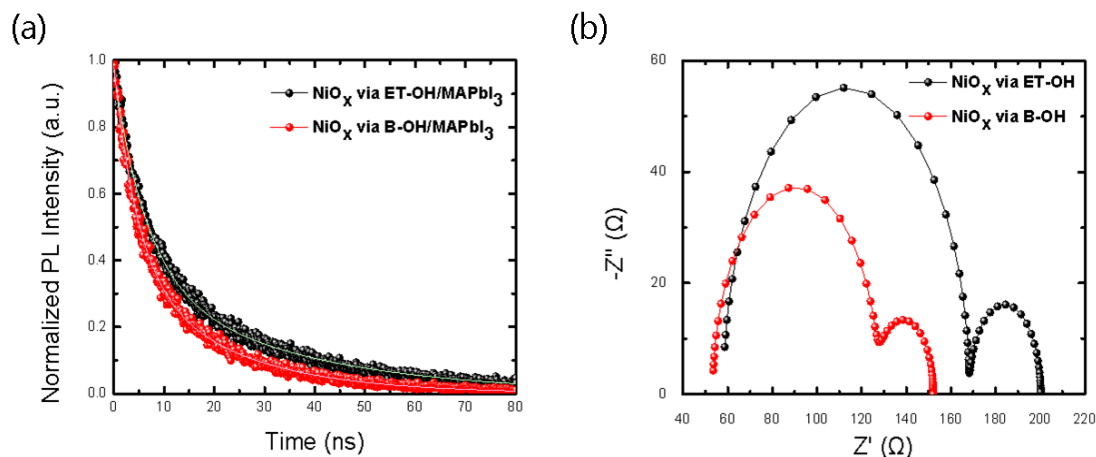


Figure 6. (a) Time-resolved transient PL spectra of glass/ NiO_x via solvent (ET-OH and B-OH)/MAPbI₃ substrate. The steady-state PL spectra were excited at a wavelength of 454 nm. (b) Dark impedance measurements of NiO_x via solvent (ET-OH and B-OH) based perovskite solar cells at V_{oc} , DC bias. The dark DC bias is applied to obtain the most efficient charge extraction results with the smallest charge transport resistance in a NiO_x via B-OH based device.

Table 3. Parameters of the TRPL (Time-Resolved Photo Luminescence) spectra and impedance.

NiO_x via Solvent	τ_1 (ns)	τ_2 (ns)	τ_{avg} (ns)	Fraction 1 (%)	Fraction 2 (%)	R_{s1} (Ω)	R_{s2} (Ω)
ET-OH	6.42	31.91	24.9	0.72	0.38	1.10×10^2	3.20×10^1
B-OH	4.67	20.41	16.07	0.68	0.41	7.45×10^1	2.43×10^1

As shown in Figure 6b and Table 3, the impedance results were analyzed using a PSC. This was carried out with reference to the circuit diagram in an earlier study [88]. The series resistances (R_s , charge transport resistance) were $7.45 \times 10^1 \Omega$ (R_{s1}) and $2.43 \times 10^1 \Omega$ (R_{s2}), which were lower in the “NiO_x via B-OH” devices than those in the “NiO_x via ET-OH” devices. Therefore, this is consistent with the device performance results, which show an improved J_{sc} and PCE (%), as shown in Table 1 [89–91].

Figure S5a,b shows a stable device operation over 1200 h and relatively high durability was confirmed in NiO_x via B-OH based cell. Additionally, statistical analysis of device performance showed that the average PCE (%) was superior to that of the comparative group. (Table S2). Thus, it was confirmed that solvent selectivity is important in NiO_x sol-gel synthesis, based on the device performance data. The device also showed a PCE (%) difference of 1.48% compared with that for PEDOT:PSS (Table 1), indicating that it can be used as a material comparable to PEDOT:PSS.

4. Conclusions

Catalyst (stabilizer)-free and reproducible NiO_x sol-gels were synthesized by selecting three organic solvents with different chain lengths of dihydric alcohols (hydroxyl groups, -diols). A transparent ITO/NiO_x substrate was applied as an HTL, using the NiO_x sol-gels to fabricate inverted PSCs. The interfacial contact of NiO_x/MAPbI₃ and the electrical characterization results showed significantly improved properties in NiO_x via B-OH, compared with those of the comparative group. Therefore, this study shows a new effect of NiO_x thin film depending on the chain length of various solvents for efficient hole charge transfer on PSCs without catalyst. Furthermore, this study has shown that the optimized NiO_x material can be used as an HTL in place of acidic PEDOT:PSS, which is expected to be a promising stepping stone in the study of metal oxide interlayers.

Supplementary Materials: The following are available online at <http://www.mdpi.com/2073-4360/10/11/1227/s1>, Figure S1: photographs of NiO_x via solvents: (a) ET-OH, (b) B-OH, and (c) P-OH sol-gel solutions and ITO/NiO_x via solvents, (d) ET-OH, (e) B-OH, and (f) P-OH substrates, Figure S2: absorbance spectra of (a) ITO/NiO_x via solvents (ET-OH, B-OH, and P-OH) and (b) glass/NiO_x via solvents (ET-OH, B-OH, and P-OH)/MAPbI₃ based on air reference, Figure S3: XRD patterns of glass/ITO/NiO_x via solvents (ET-OH, B-OH, and P-OH), Figure S4: the contact angle images of water droplet (H₂O) on different surfaces: (a) glass /NiO_x via ET-OH, (b) glass/NiO_x via B-OH, and (c) glass /NiO_x via P-OH, Figure S5: (a) histogram of PCE (%) device performance for 20 perovskite solar cells fabricated under NiO_x via solvent control, (b) Normalized PCE (%) of a perovskite solar cell containing HTLs of NiO_x via ET-OH (black) and B-OH (red) measured under ambient environmental conditions and standard AM 1.5 solar illumination, Table S1: basic properties of the three solvents used in NiO_x sol-gel synthesis, Table S2: PCE (%) statistical data of perovskite solar cells based on NiO_x via solvent.

Author Contributions: Conceptualization, B.G.K.; methodology and analysis, B.G.K., and W.J.; writing—original draft preparation B.G.K., and D.H.W.; writing—review and editing, B.G.K., W.J., and D.H.W.

Funding: This research was supported by the Basic Science Research Program, through the National Research Foundation (NRF) of Korea, funded by the Ministry of Science, ICT & Future Planning (2017R1A1A1A05000772). This research was also supported by the Technology Innovation Program (no. 20000508, ‘Development of Superelastic Alloy Electrode Based Photovoltaic Fiber’) funded by the Ministry of Trade, Industry & Energy (MOTIE, Korea).

Conflicts of Interest: The authors declare no conflicts of interest.

References

1. Uddin, A. Perovskite Solar Cells. In *World Scientific Handbook of Organic Optoelectronic Devices*; Huang, J., Yuan, Y., Eds.; World Scientific: Munich, Germany, 2018; pp. 285–367.
2. Di Girolamo, D.; Matteocci, F.; Lamanna, E.; Calabrò, E.; Di Carlo, A.; Dini, D. Inverted perovskite solar cells with transparent hole transporting layer based on semiconducting nickel oxide. *AIP Conf. Proc.* **2018**, *1990*, 020011. [[CrossRef](#)]
3. Lee, D.S.; Yun, J.S.; Kim, J.; Soufiani, A.M.; Chen, S.; Cho, Y.; Deng, X.; Seidel, J.; Lim, S.; Huang, S.; et al. Passivation of Grain Boundaries by Phenethylammonium in Formamidinium-Methylammonium Lead Halide Perovskite Solar Cells. *ACS Energy Lett.* **2018**, *3*, 647–654. [[CrossRef](#)]

4. NREL. Best Research Cell Efficiency Chart. National Renewable Energy Laboratory: Golden, CO, USA, 2018. Available online: <https://www.nrel.gov/pv/assets/pdfs/pv-efficiencies-07-17-2018.pdf> (accessed on 17 July 2017).
5. Huang, Z.; Wang, D.; Wang, S.; Zhang, T. Highly Efficient and Stable MAPbI₃ Perovskite Solar Cell Induced by Regulated Nucleation and Ostwald Recrystallization. *Materials* **2018**, *11*, 778. [[CrossRef](#)] [[PubMed](#)]
6. Zhou, W.; Zhou, P.; Lei, X.; Fang, Z.; Zhang, M.; Liu, Q.; Chen, T.; Zeng, H.; Ding, L.; Zhu, J.; et al. Phase Engineering of Perovskite Materials for High-Efficiency Solar Cells: Rapid Conversion of CH₃NH₃PbI₃ to Phase-Pure CH₃NH₃PbCl₃ via Hydrochloric Acid Vapor Annealing Post-Treatment. *ACS Appl. Mater. Interfaces* **2018**, *10*, 1897–1908. [[CrossRef](#)] [[PubMed](#)]
7. Cui, J.; Yuan, H.; Li, J.; Xu, X.; Shen, Y.; Lin, H.; Wang, M. Recent progress in efficient hybrid lead halide perovskite solar cells. *Sci. Technol. Adv. Mater.* **2015**, *16*, 036004. [[CrossRef](#)] [[PubMed](#)]
8. Pang, S.; Li, X.; Dong, H.; Chen, D.; Zhu, W.; Chang, J.; Lin, Z.; Xi, H.; Zhang, J.; Zhang, C.; et al. Efficient Bifacial Semitransparent Perovskite Solar Cells Using Ag/V₂O₅ as Transparent Anodes. *ACS Appl. Mater. Interfaces* **2018**, *10*, 12731–12739. [[CrossRef](#)] [[PubMed](#)]
9. Pang, S.; Chen, D.; Zhang, C.; Chang, J.; Lin, Z.; Yang, H.; Sun, X.; Mo, J.; Xi, H.; Han, G.; et al. Efficient bifacial semitransparent perovskite solar cells with silver thin film electrode. *Sol. Energy Mater. Sol. Cells* **2017**, *170*, 278–286. [[CrossRef](#)]
10. Yang, H.; Zhang, J.; Zhang, C.; Chang, J.; Lin, Z.; Chen, D.; Xi, H.; Hao, Y.; Yang, H.; Zhang, J.; et al. Effects of Annealing Conditions on Mixed Lead Halide Perovskite Solar Cells and Their Thermal Stability Investigation. *Materials* **2017**, *10*, 837. [[CrossRef](#)] [[PubMed](#)]
11. Sun, X.; Zhang, C.; Chang, J.; Yang, H.; Xi, H.; Lu, G.; Chen, D.; Lin, Z.; Lu, X.; Zhang, J.; et al. Mixed-solvent-vapor annealing of perovskite for photovoltaic device efficiency enhancement. *Nano Energy* **2016**, *28*, 417–425. [[CrossRef](#)]
12. Mo, J.; Zhang, C.; Chang, J.; Yang, H.; Xi, H.; Chen, D.; Lin, Z.; Lu, G.; Zhang, J.; Hao, Y. Enhanced efficiency of planar perovskite solar cells via a two-step deposition using DMF as an additive to optimize the crystal growth behavior. *J. Mater. Chem. A* **2017**, *5*, 13032–13038. [[CrossRef](#)]
13. Yang, H.; Zhang, J.; Zhang, C.; Chang, J.; Lin, Z.; Chen, D.; Sun, X.; Xi, H.; Han, G.; Hao, Y. Effect of polyelectrolyte interlayer on efficiency and stability of p-i-n perovskite solar cells. *Sol. Energy* **2016**, *139*, 190–198. [[CrossRef](#)]
14. Liu, T.; Chen, K.; Hu, Q.; Zhu, R.; Gong, Q. Inverted Perovskite Solar Cells: Progresses and Perspectives. *Adv. Energy Mater.* **2016**, *6*, 1600457. [[CrossRef](#)]
15. Yang, W.S.; Park, B.-W.; Jung, E.H.; Jeon, N.J.; Kim, Y.C.; Lee, D.U.; Shin, S.S.; Seo, J.; Kim, E.K.; Noh, J.H.; et al. Iodide management in formamidinium-lead-halide-based perovskite layers for efficient solar cells. *Science* **2017**, *356*, 1376–1379. [[CrossRef](#)] [[PubMed](#)]
16. Rong, Y.; Hu, Y.; Mei, A.; Tan, H.; Saidaminov, M.I.; Seok, S.; McGehee, M.D.; Sargent, E.H.; Han, H. Challenges for commercializing perovskite solar cells. *Science* **2018**, *361*, eaat8235. [[CrossRef](#)] [[PubMed](#)]
17. Pitchaiya, S.; Natarajan, M.; Santhanam, A.; Asokan, V.; Yuvapragasam, A.; Madurai Ramakrishnan, V.; Palanisamy, S.E.; Sundaram, S.; Velauthapillai, D. A review on the classification of organic/inorganic/carbonaceous hole transporting materials for perovskite solar cell application. *Arab. J. Chem.* **2018**. [[CrossRef](#)]
18. Li, M.-H.; Yum, J.-H.; Moon, S.-J.; Chen, P.; Li, M.-H.; Yum, J.-H.; Moon, S.-J.; Chen, P. Inorganic p-Type Semiconductors: Their Applications and Progress in Dye-Sensitized Solar Cells and Perovskite Solar Cells. *Energies* **2016**, *9*, 331. [[CrossRef](#)]
19. Yu, Z.; Sun, L. Inorganic Hole-Transporting Materials for Perovskite Solar Cells. *Small Methods* **2018**, *2*, 1700280. [[CrossRef](#)]
20. Arora, N.; Dar, M.I.; Hinderhofer, A.; Pellet, N.; Schreiber, F.; Zakeeruddin, S.M.; Grätzel, M. Perovskite solar cells with CuSCN hole extraction layers yield stabilized efficiencies greater than 20. *Science* **2017**, *358*, 768–771. [[CrossRef](#)] [[PubMed](#)]
21. Zimmermann, E.; Wong, K.K.; Müller, M.; Hu, H.; Ehrenreich, P.; Kohlstädt, M.; Würfel, U.; Mastroianni, S.; Mathiazhagan, G.; Hinsch, A.; et al. Characterization of perovskite solar cells: Towards a reliable measurement protocol. *APL Mater.* **2016**, *4*, 091901. [[CrossRef](#)]
22. Chen, B.; Yang, M.; Priya, S.; Zhu, K. Origin of J–V Hysteresis in Perovskite Solar Cells. *J. Phys. Chem. Lett.* **2016**, *7*, 905–917. [[CrossRef](#)] [[PubMed](#)]

23. Duc Duong, T. Development of High Efficiency Four-Terminal Perovskite-Silicon Tandems. Ph.D. Thesis, The Australian National University, Canberra, Australia, July 2017.
24. Qiu, L.; Ono, L.K.; Qi, Y. Advances and challenges to the commercialization of organic–inorganic halide perovskite solar cell technology. *Mater. Today Energy* **2018**, *7*, 169–189. [[CrossRef](#)]
25. Tonui, P.; Oseni, S.O.; Sharma, G.; Mola, G.T.; Oseni, S.O.; Yan, Q.; Tessema Mola, G. Perovskites photovoltaic solar cells: An overview of current status. *Renew. Sustain. Energy Rev.* **2018**, *91*, 1025–1044. [[CrossRef](#)]
26. Savva, A.; Papadas, I.T.; Tsikritzis, D.; Armatas, G.S.; Kennou, S.; Choulis, S.A. Room Temperature Nanoparticulate Interfacial Layers for Perovskite Solar Cells via solvothermal synthesis. *J. Mater. Chem. A* **2017**, *5*, 20381–20389. [[CrossRef](#)]
27. Fan, J.; Jia, B.; Gu, M. Perovskite-based low-cost and high-efficiency hybrid halide solar cells. *Photonics Res.* **2014**, *2*, 111–120. [[CrossRef](#)]
28. Guo, Y.; Lei, H.; Xiong, L.; Li, B.; Fang, G. An integrated organic–inorganic hole transport layer for efficient and stable perovskite solar cells. *J. Mater. Chem. A* **2018**, *6*, 2157–2165. [[CrossRef](#)]
29. Chang, C.-C.; Tao, J.-H.; Tsai, C.-E.; Cheng, Y.-J.; Hsu, C.-S. Cross-linked Triarylamine-Based Hole-Transporting Layer for Solution-Processed PEDOT:PSS-Free Inverted Perovskite Solar Cells. *ACS Appl. Mater. Interfaces* **2018**, *10*, 21466–21471. [[CrossRef](#)] [[PubMed](#)]
30. Zheng, J.; Hu, L.; Yun, J.S.; Zhang, M.; Lau, C.F.J.; Bing, J.; Deng, X.; Ma, Q.; Cho, Y.; Fu, W.; et al. Solution-Processed, Silver-Doped NiO_x as Hole Transporting Layer for High-Efficiency Inverted Perovskite Solar Cells. *ACS Appl. Energy Mater.* **2018**, *1*, 561–570. [[CrossRef](#)]
31. Pérez-Tomás, A.; Mingorance, A.; Tanenbaum, D.; Lira-Cantú, M. Metal Oxides in Photovoltaics: All-Oxide, Ferroic, and Perovskite Solar Cells. In *The Future of Semiconductor Oxides in Next-Generation Solar Cells*; Lira-Cantu, M., Ed.; Elsevier: Amsterdam, The Netherlands, 2018; pp. 267–356.
32. Kumar Elumalai, N.; Vijila, C.; Jose, R.; Uddin, A.; Ramakrishna, S. Metal oxide semiconducting interfacial layers for photovoltaic and photocatalytic applications. *Mater. Renew. Sustain. Energy* **2015**, *4*, 11. [[CrossRef](#)]
33. Livage, J.; Ganguli, D. Sol–gel electrochromic coatings and devices: A review. *Sol. Energy Mater. Sol. Cells* **2001**, *68*, 365–381. [[CrossRef](#)]
34. Koplick, A.J.; Jenkins, S.M. Preparation of Metal Alkoxides. U.S. Patent 09530858, 6 November 1998.
35. Omaima, A.M. Metal Alkoxides as Starting Materials for Hydrolysis Processes. Master’s Thesis, Department of Chemistry, Faculty of Education, University of Khartoum, Khartoum State, Sudan, December 1999.
36. Enggrob, M.; Gydesen, E.; Simonsen, M.E.; Søgaard, E.G. Aalborg Universitet Sol-gel reactions of titanium alkoxides and water: Influence of pH and alkoxy group on cluster formation and properties of the resulting products Sol-gel reactions of titanium alkoxides and water: Influence of pH and alkoxy group on cluster formation and properties of the resulting products. *J. Sol-Gel Sci. Technol.* **2010**, *53*, 485–497. [[CrossRef](#)]
37. Okamoto, T.; Ichino, R.; Okido, M.; Liu, Z.; Zhang, C. Effect of Ammonia on the Crystal Morphology of Nickel Oxalate Precipitates and their Thermal Decomposition into Metallic Nickel. *Mater. Trans.* **2005**, *46*, 171–174. [[CrossRef](#)]
38. Hasan, M.; Drazin, J.; Dey, S.; Castro, R.H.R. Synthesis of stoichiometric nickel aluminate spinel nanoparticles. *Am. Mineral.* **2015**, *100*, 652–657. [[CrossRef](#)]
39. He, L.-H.; Zhao, Z.-W.; Zhang, Y.-X. Synthesis of nickel ferrite precursors from low grade nickel matte. *Trans. Nonferrous Met. Soc. China* **2013**, *23*, 2422–2430. [[CrossRef](#)]
40. Edward, P.; Ramakumar, A.; Alexandra, N.; Donald, L.S. Nickel Solubility and Precipitation in Soils: A Thermodynamic Study. *Clays Clay Miner.* **2006**, *54*, 153–164. [[CrossRef](#)]
41. Okamoto, T.; Yang, J.G.; Kuroda, K.; Ichino, R.; Okido, M. Preparation of Size and Aggregation Controlled Nickel Oxalate Dihydrate Particles From Nickel Hydroxide. *Adv. Mater. Res.* **2014**, *15–17*, 581–586. [[CrossRef](#)]
42. Dean, F. Chelation Compositions. U.S. Patent 6870026B1, 22 March 2005.
43. Mohammadi, E.; Aliofkhaezai, M.; Hasanpoor, M.; Chipara, M. Hierarchical and Complex ZnO Nanostructures by Microwave-Assisted Synthesis: Morphologies, Growth Mechanism and Classification. *Crit. Rev. Solid State Mater. Sci.* **2018**, *43*, 475–541. [[CrossRef](#)]
44. Koschnick, T.J.; Haller, W.T. Effects of Copper Chelating Agents on Diquat Activity in Diquat Resistant Landoltia. *J. Aquat. Plant Manag.* **2006**, *44*, 125–132.
45. Zhang, Q.; Sando, D.; Nagarajan, V. Chemical Route derived Bismuth Ferrite Thin films and Nanomaterials. *J. Mater. Chem. C* **2016**, *4*, 4092–4124. [[CrossRef](#)]

46. Cabanas-Polo, S.; Ferrari, B.; Sánchez-Herencia, A.J. Colloidal stability of Ni(OH)₂ in water and its dispersion into a ceramic matrix from the reaction media to obtain Ni/Al₂O₃ materials. *Bol. Soc. Esp. Ceram. Vidrio* **2014**, *53*, 265–274. [CrossRef]
47. Munnik, P.; De Jongh, P.E.; De Jong, K.P. Recent Developments in the Synthesis of Supported Catalysts. *Chem. Rev.* **2015**, *115*, 6687–6718. [CrossRef] [PubMed]
48. Majewski, A.J.; Wood, J.; Bujalski, W. Nickel–silica core@shell catalyst for methane reforming. *Int. J. Hydrogen Energy* **2013**, *38*, 14531–14541. [CrossRef]
49. Imran Din, M.; Rani, A. Recent Advances in the Synthesis and Stabilization of Nickel and Nickel Oxide Nanoparticles: A Green Adeptness. *Int. J. Anal. Chem.* **2016**, *2016*, 1–14. [CrossRef] [PubMed]
50. De, S.; Zhang, J.; Luque, R.; Yan, N. Ni-based bimetallic heterogeneous catalysts for energy and environmental applications. *Energy Environ. Sci.* **2016**, *9*, 3314–3347. [CrossRef]
51. Talbot, F.J.; Richard R De, B.; Powell, B.E.; Nobbe, L.B. Boiling Point Determination. U.S. Patent 3216239A, 9 November 1965.
52. Benham, S. Experiments on Evaporation & Surface Area. Available online: <https://sciencing.com/experiments-evaporation-surface-area-10041602.html> (accessed on 26 September 2018).
53. Intermolecular and Interatomic Forces. Available online: <https://intl.siyavula.com/read/science/grade-11/intermolecular-forces/04-intermolecular-forces-01> (accessed on 26 September 2018).
54. Paquet, C.; Lacelle, T.; Liu, X.; Deore, B.; Kell, A.J.; Lafrenière, S.; Malenfant, P.R.L. The role of amine ligands in governing film morphology and electrical properties of copper films derived from copper formate-based molecular inks. *Nanoscale* **2018**, *10*, 6911–6921. [CrossRef] [PubMed]
55. Lee, J.-H.; Kim, S.; Kim, H.; Lee, J. Solvent-dependent performance of solution-processed small-molecule organic field-effect transistors. *Org. Electron.* **2018**, *52*, 184–189. [CrossRef]
56. Lasprilla-Botero, J.; Álvarez-Láinez, M.; Lagaron, J.M. The influence of electrospinning parameters and solvent selection on the morphology and diameter of polyimide nanofibers. *Mater. Today Commun.* **2018**, *14*, 1–9. [CrossRef]
57. Carey, V.P. *Liquid-Vapor Phase-Change Phenomena: An Introduction to the Thermophysics of Vaporization and Condensation Processes in Heat Transfer Equipment*; Taylor and Francis Group, LLC: New York, NY, USA, 2008; ISBN 1351434861.
58. Mugheirbi, N.A.; Mosquera-Giraldo, L.I.; Borca, C.H.; Slipchenko, L.V.; Taylor, L.S. Phase Behavior of Drug-Hydroxypropyl Methylcellulose Amorphous Solid Dispersions Produced from Various Solvent Systems: Mechanistic Understanding of the Role of Polymer using Experimental and Theoretical Methods. *Mol. Pharm.* **2018**, *15*, 3236–3251. [CrossRef] [PubMed]
59. Song, Z.; Chiang, S.W.; Chu, X.; Du, H.; Li, J.; Gan, L.; Xu, C.; Yao, Y.; He, Y.; Li, B.; et al. Effects of solvent on structures and properties of electrospun poly(ethylene oxide) nanofibers. *J. Appl. Polym. Sci.* **2018**, *135*, 45787. [CrossRef]
60. Steirer, K.X.; Richards, R.E.; Sigdel, A.K.; Garcia, A.; Ndione, P.F.; Hammond, S.; Baker, D.; Ratcliff, E.L.; Curtis, C.; Furtak, T.; et al. Nickel oxide interlayer films from nickel formate–ethylenediamine precursor: Influence of annealing on thin film properties and photovoltaic device performance. *J. Mater. Chem. A* **2015**, *3*, 10949–10958. [CrossRef]
61. Garcia-Miquel, J.; Zhang, Q.; Allen, S.; Rougier, A.; Blyr, A.; Davies, H.; Jones, A.; Leedham, T.; Williams, P.; Impey, S. Nickel oxide sol–gel films from nickel diacetate for electrochromic applications. *Thin Solid Films* **2003**, *424*, 165–170. [CrossRef]
62. Sumida, K.; Liang, K.; Reboul, J.; Ibarra, I.A.; Furukawa, S.; Falcaro, P. Sol–Gel Processing of Metal–Organic Frameworks. *Chem. Mater.* **2017**, *29*, 2626–2645. [CrossRef]
63. Liu, F.; Wu, J.; Chen, K.; Xue, D. Morphology Study by Using Scanning Electron Microscopy. *Microsc. Sci. Technol. Appl. Educ.* **2010**, 1781–1792.
64. Eugene, A.; Mariagoretti, U.; Samuel, A. A Review on Synthetic Methods of Nanostructured Materials. *Chem. Res. J.* **2017**, *2*, 97–123.
65. Wang, N.; Sun, X. Perovskite Thin Films Having Large Crystalline Grains. U.S. Patent 20160254472A1, 1 September 2016.
66. Ogundana, I.J.; Foo, S.Y. Improving the Morphology of the Perovskite Absorber Layer in Hybrid Organic/Inorganic Halide Perovskite MAPbI₃ Solar Cells. *J. Sol. Energy* **2017**, *2017*, 1–9. [CrossRef]

67. Wu, Y.; Chen, W.; Yue, Y.; Liu, J.; Bi, E.; Yang, X.; Islam, A.; Han, L. Consecutive Morphology Controlling Operations for Highly Reproducible Mesoporous Perovskite Solar Cells. *ACS Appl. Mater. Interfaces* **2015**, *7*, 20707–20713. [[CrossRef](#)] [[PubMed](#)]
68. Chen, B.; Chen, S.; Dong, B.; Gao, X.; Xiao, X.; Zhou, J.; Hu, J.; Tang, S.; Yan, K.; Hu, H.; et al. Electrical Heating-Assisted Multiple Coating Method for Fabrication of High-Performance Perovskite Fiber Solar Cells by Thickness Control. *Adv. Mater. Interfaces* **2017**, *4*, 1700833. [[CrossRef](#)]
69. Ulkuniemi, M. Influence of Processing Conditions on the Performance of Perovskite Solar Cells. Master's Thesis, University of Oulu, Oulu, Finland, November 2017.
70. Fachbereich, I.; Kirill, M.S.; Aus, Z. Solution-Processed Charge Extraction Interlayers and Electrodes for Organic Solar Cells. Master's Thesis, The University of Wuppertal, Wuppertal, Germany, July 2014.
71. Wing, D. The Selection and Optimization of Transparent Conducting Oxides for Electrodes in Polymer Solar Cells. Research Thesis, Israel Institute of Technology, Haifa, Israel, May 2014.
72. Ferguson, T.P. Jianmin Qu Moisture and temperature effects on the reliability of interfacial adhesion of a polymer/metal interface. In Proceedings of the 54th Electronic Components and Technology Conference, Las Vegas, NV, USA, 4–4 June 2004; pp. 1752–1758.
73. Chen, L.-C.; Lin, Y.-S.; Tseng, Z.-L.; Wu, C.; Kao, F.-S.; Chen, S.-H.; Chen, L.-C.; Lin, Y.-S.; Tseng, Z.-L.; Wu, C.; et al. Overcoming the Intrinsic Difference between Hydrophilic CH₃NH₃PbI₃ and Hydrophobic C60 Thin Films to Improve the Photovoltaic Performance. *Nanomaterials* **2017**, *7*, 166. [[CrossRef](#)] [[PubMed](#)]
74. Murali, B.; Yengel, E.; Yang, C.; Peng, W.; Alarousu, E.; Bakr, O.M.; Mohammed, O.F. The Surface of Hybrid Perovskite Crystals: A Boon or Bane. *ACS Energy Lett.* **2017**, *2*, 846–856. [[CrossRef](#)]
75. Xu, X.; Liu, Z.; Zuo, Z.; Zhang, M.; Zhao, Z.; Shen, Y.; Zhou, H.; Chen, Q.; Yang, Y.; Wang, M. Hole Selective NiO Contact for Efficient Perovskite Solar Cells with Carbon Electrode. *Nano Lett.* **2015**, *15*, 2402–2408. [[CrossRef](#)] [[PubMed](#)]
76. Song, T.-B.; Chen, Q.; Zhou, H.; Jiang, C.; Wang, H.-H.; Yang, Y.; Liu, Y.; You, J.; Yang, Y. Perovskite solar cells: Film formation and properties. *J. Mater. Chem. A* **2015**, *3*, 9032–9050. [[CrossRef](#)]
77. Hettiarachchi, C.L. Organolead Halide Perovskite Solar Absorbers and Ferroelectric Nanocomposites for Harvesting Solar Energy Perovskite Solar Cells View Project Quantum Dot Solar Cells View Project. Ph.D. Thesis, University of South Florida, Tampa, FL, USA, April 2018.
78. Tamura, H.; Burghardt, I. Ultrafast charge separation in organic photovoltaics enhanced by charge delocalization and vibronically hot exciton dissociation. *J. Am. Chem. Soc.* **2013**, *135*, 16364–16367. [[CrossRef](#)] [[PubMed](#)]
79. Janković, V.J.; Vukmirović, N. Identification of Ultrafast Photophysical Pathways in Photoexcited Organic Heterojunctions. *J. Am. Chem. Soc.* **2017**, *121*, 19602–19618. [[CrossRef](#)]
80. Yang, Z.; Wang, M.; Qiu, H.; Yao, X.; Lao, X.; Xu, S.; Lin, Z.; Sun, L.; Shao, J. Engineering the Exciton Dissociation in Quantum-Confined 2D CsPbBr₃ Nanosheet Films. *Adv. Funct. Mater.* **2018**, *28*, 1705908. [[CrossRef](#)]
81. Dimitrov, S.D.; Nielsen, C.B.; Shoaee, S.; Shakya Tuladhar, P.; Du, J.; McCulloch, I.; Durrant, J.R. Efficient Charge Photogeneration by the Dissociation of PC₇₀ BM Excitons in Polymer/Fullerene Solar Cells. *J. Phys. Chem. Lett.* **2012**, *3*, 140–144. [[CrossRef](#)]
82. Paulke, A.; Stranks, S.D.; Kniepert, J.; Kurpiers, J.; Wolff, C.M.; Schön, N.; Snaith, H.J.; Brenner, T.J.K.; Neher, D. Charge carrier recombination dynamics in perovskite and polymer solar cells; Charge carrier recombination dynamics in perovskite and polymer solar cells. *Appl. Phys. Lett.* **2016**, *108*, 103102. [[CrossRef](#)]
83. Ponseca, C.S.; Tian, Y.; Sundström, V.; Scheblykin, I.G. Excited state and charge-carrier dynamics in perovskite solar cell materials. *Nanotechnology* **2016**, *27*, 082001. [[CrossRef](#)] [[PubMed](#)]
84. Peng, J.; Chen, Y.; Zheng, K.; Pullerits, T.; Liang, Z. Insights into charge carrier dynamics in organo-metal halide perovskites: From neat films to solar cells. *Chem. Soc. Rev.* **2017**, *46*, 5714–5729. [[CrossRef](#)] [[PubMed](#)]
85. Shi, D.; Adinolfi, V.; Comin, R.; Yuan, M.; Alarousu, E.; Buin, A.; Chen, Y.; Hoogland, S.; Rothenberger, A.; Katsiev, K.; et al. Low trap-state density and long carrier diffusion in organolead trihalide perovskite single crystals. *Science* **2015**, *347*, 519–522. [[CrossRef](#)] [[PubMed](#)]
86. Zhou, Y.; Fuentes-Hernandez, C.; Shim, J.; Meyer, J.; Giordano, A.J.; Li, H.; Winget, P.; Papadopoulos, T.; Cheun, H.; Kim, J.; et al. A universal method to produce low-work function electrodes for organic electronics. *Science* **2012**, *336*, 327–332. [[CrossRef](#)] [[PubMed](#)]

87. Stranks, S.D.; Eperon, G.E.; Grancini, G.; Menelaou, C.; Alcocer, M.J.P.; Leijtens, T.; Herz, L.M.; Petrozza, A.; Snaith, H.J. Electron-hole diffusion lengths exceeding 1 micrometer in an organometal trihalide perovskite absorber. *Science* **2013**, *342*, 341–344. [[CrossRef](#)] [[PubMed](#)]
88. Galatopoulos, F.; Savva, A.; Papadas, I.T.; Choulis, S.A. The Effect of Hole Transporting Layer in Charge Accumulation Properties of p-i-n Perovskite Solar Cells. *APL Mater.* **2017**, *5*, 076102. [[CrossRef](#)]
89. Li, Y.; Ding, B.; Chu, Q.-Q.; Yang, G.-J.; Wang, M.; Li, C.-X.; Li, C.-J. Ultra-high open-circuit voltage of perovskite solar cells induced by nucleation thermodynamics on rough substrates. *Sci. Rep.* **2017**, *7*, 46141. [[CrossRef](#)] [[PubMed](#)]
90. Zhang, L.; Liu, T.; Liu, L.; Hu, M.; Yang, Y.; Mei, A.; Han, H. The effect of carbon counter electrodes on fully printable mesoscopic perovskite solar cells. *J. Mater. Chem. A* **2015**, *3*, 9165–9170. [[CrossRef](#)]
91. Yadav, P.; Prochowicz, D.; Saliba, M.; Boix, P.; Zakeeruddin, S.; Grätzel, M.; Yadav, P.; Prochowicz, D.; Saliba, M.; Boix, P.P.; et al. Interfacial Kinetics of Efficient Perovskite Solar Cells. *Crystals* **2017**, *7*, 252. [[CrossRef](#)]



© 2018 by the authors. Licensee MDPI, Basel, Switzerland. This article is an open access article distributed under the terms and conditions of the Creative Commons Attribution (CC BY) license (<http://creativecommons.org/licenses/by/4.0/>).